Coupling Mechanisms for the Localization Module of NeuralSemantic SLAM

Alicia Bremer

Abstract

One issue with current models of path integration in the brain, which seek to model how estimates of position are maintained during motion, is that the estimate drifts from the true path without outside correction. In the localization module of the NeuralSemantic SLAM, which performs path integration, the location information is stored as a high-dimensional vector with structured properties (Dumont et al. 2023). This project investigates methods for correcting the location estimate based on relationships between the components of its encoding. I implement three different coupling mechanisms using spiking neurons, which extend the localization module. In my experiments, I compare the error with and without the coupling mechanisms, varying the number of neurons in the model. Since this module is implemented with spiking neurons, I also look at the spiking activity of the neurons. Adding coupling mechanisms to the localization module resulted in larger error measurements overall. For two of the three coupling mechanisms, increasing the number of neurons did not improve the error. Due to this increased error, these results suggest that the coupling mechanisms that I implemented have not improved the path integrator. However, further extensions to these coupling mechanisms, such as reducing the extent of correction, may be able to improve the accuracy of the localization module.

1 Introduction

The NeuralSemantic SLAM model is a collection of spiking neural networks which together perform simultaneous localization and mapping (SLAM). The goal with developing this model was to better understand how spatial navigation occurs in the brain. Thus, the NeuralSemantic SLAM model is biologically constrained and uses representations of spatial information consistent with neuroscience findings (Dumont et al. 2023).

One of the main modules of the NeuralSemanticSLAM is the localization module (LM), which consists of a path integrator (PI) model and grid cell population. The spatial information encoded in the LM drifts without input from the rest of the SLAM system. This project investigates different mechanisms to reduce drift in the LM.

There has been a significant amount of previous research into the problem of path integration

in the brain, as well as SLAM. Since this project focuses on extending the PI model of the NeuralSemantic SLAM model, I will specifically focus on the research in this area.

The discovery of place cells in the hippocampus and grid cells in the entorhinal cortex (EC) led to a much deeper understanding of spatial navigation in the brain. Place cells in the hippocampus fire when an animal is in a specific location of the environment. These cells may also fire in a different environment when an animal is in a specific location, and this location may not be correlated to the first environment (Moser et al. 2008).

Grid cells in the EC have also been discovered which fire when an animal is in specific regions of the environment. Grid cells may fire when an animal is in different areas of the environment. These regions form a repeating triangular grid which cover the environment. Different grid cells have different grids, which enable grid cells to represent the environment (Moser et al. 2008).

In addition to grid cells, other cells have been discovered in the EC. In the deeper layers of the EC, there are cells which fire when the head is moving in a specific direction. The locations of these cells overlap with the grid cells in deeper layers of the EC. The appearance of grid cells and head-direction cells together has been suggested to enable path integration (Sargolini et al. 2006). The repetition in the information encoded by the grid cells suggests that this information may be able to be used in an algorithmic way. There also exist direct perforant pathways from the cells in layers II and III of the EC to the hippocampus, underlining the connection between grid cells in the EC to place cells in the hippocampus (Moser et al. 2008).

The discovery of place cells and grid cells have led to various models of path integration. There are two main proposed PI models. The first type of model are oscillatory-interference (OI) models. These models propose that there are components in the EC which oscillate at a frequency which is controlled by velocity - that is, Velocity-Controlled Oscillators (VCOs). Moreover, the relation between the encoded information of the VCOs and Fourier theory suggests that the brain may use Fourier coefficients to encode spatial information (Orchard et al. 2013).

The other type of model is continuous attractor network (CAN) models, which are recurrently connected networks which store the position of the animal as a bump. Connecting to the neuroscience discussions above, these networks may be realized deeper layers of the EC, where there are many recurrent connections (McNaughton et al. 2006).

There are numerous constraints placed on PI models. One constraint is that these models demonstrate the periodic firing pattern of the grid cells, which is a prominent feature of the encoding of spatial information. However, there are also other constraints.

In addition to the EC, grid cells and head-direction cells have been found in other areas around the hippocampus, such as the presubiculum and parasubiculum. These regions have different distributions of grid cells compared to the EC, as the grid cells are evenly distributed throughout (Boccara et al. 2010). Ideally, grid cell-based PI models can still explain the appearance of grid cells in areas other than the EC.

Another biological constraint is the number of cells influenced by direction and velocity.

There are many more grid cells in the layers of the deep EC than cells which are influenced by direction (Moser et al. 2008). While these discoveries about conjunctive cells in the deep EC do suggest that some grid cells may also be sensitive to direction (Sargolini et al. 2006), this biological constraint exists. One major limitation of OI models is that this distribution of grid cells compared to velocity-controlled cells differs. Since our understanding of the deeper layers of the EC is still limited, there may be VCOs which do exist in these layers. However, there is minimal current neuroscience evidence which supports this view.

A neuroscience study measuring the membrane potentials of neurons in the EC suggests that a hybrid model between an OI model and a CAN model may best explain the findings. The study found that the membrane of the grid cells in the EC depolarized slowly, which the authors noted is a behaviour displayed by CAN models, while also exhibiting phase activity that can be explained by an OI model (Schmidt-Hieber and Haeusser 2013).

The PI component of the NeuralSemantic SLAM, which was developed before the NeuralSemantic SLAM, is a hybrid model which has elements of both OI models and CAN models. This model uses VCOs to update the position estimate and attractor dynamics for stability (Dumont et al. 2022). The VCOs themselves do not display grid-cell like activity, and instead banded activity which is similar to activity predicted by other OI models (Burgess 2008). However, the information can be decoded and cleaned up to a grid-cell like representation, which is the second component of the LM in the NeuralSemantic SLAM. The specific components of both the PI component and the grid cells of the LM of the NeuralSemantic SLAM will be discussed below in Section 2.

Coupling mechanisms have been proposed to improve the accuracy of the OI models of path integration, based on the pattern of the grid cell firing fields (Burgess and Burgess 2014) or the structure of Fourier coefficients which have been suggested store spatial information in the brain (Orchard et al. 2013). These coupling mechanisms can reduce the drift of PI models, which is necessary for OI models to be a valid explanation of the neuroscience evidence behind path integration. Path integration in the brain is stable. Although not all connections are understood, as noted previously, exploring coupling mechanisms may help in understanding the function of grid cells in path integration.

The objective of this project is to add coupling mechanisms to the LM of the NeuralSemantic SLAM to attempt to reduce drift and improve accuracy. The SLAM components of the NeuralSemantic SLAM provide error correction to the PI model, which reduces the error of the PI (Dumont et al. 2023). I am interested in investigating whether coupling mechanisms for improving the accuracy of the LM are feasible, without the rest of the SLAM components.

To understand how coupling mechanisms can be applied in the LM, I will first provide a detailed overview of the LM - including the PI model, the grid cell population and the specific encoding of spatial information. Then, I will propose different coupling mechanisms based on the grid-like firing patterns of the grid cells and their connection to Fourier coefficients.

I will then implement and test these coupling mechanisms, and compare them to the original model. The main objective is to determine whether coupling between VCOs in the PI component and/or the grid cells can improve the accuracy of the LM. Since I am interested

in the amount of drift, I will analyze the LM on various paths, and examine the resulting firing patterns of the grid cells in the LM.

One specific hypothesis I am also interested in testing is whether coupling mechanisms between the PI model and grid cells in the LM can reduce the number of neurons in VCO populations. As noted above, grid cells have been the predominant cells found so far in deeper regions of the EC. I hypothesize that adding coupling mechanisms can begin to reconcile this PI and grid cell model with the neuroscience findings on the ratio of grid cells in the hippocampal regions of the brain.

2   Methods

Before focusing on the LM, I will provide background on the way information is encoded for the model.

2.1   Encoding Information

The semantic pointer architecture (SPA) was introduced as a framework to explain cognitive processes with the idea that information is represented in processes in the brain as *semantic pointers*, which carry some information about meaning. These can be viewed as high-dimensional vectors, which are encoded in the activity of neurons (Eliasmith 2013).

The specific implementation of SPA in the NeuralSemantic SLAM is Holographic Reduced Representations (HHRs) which can be encoded in spiking neurons (Dumont et al. 2023). There are also other vector symbol architectures (VSAs) which describe ways to encode information in high-dimensional vectors (Eliasmith 2013).

There are numerous operations that have been defined and explored with semantic pointers. One is computing the similarity between two vectors, which is the dot product. Another one of the main operations is *bundling*, which is represented by + and collects semantic pointers into a set. The other main operation is binding, which is represented by ⊛ and involves combining semantic pointers into a new semantic pointer which combines the meaning of the original semantic pointers. In HRRs, this process is done with circular convolution. Unbinding approximately reverses this process. With HRRs, unbinding is done with an approximate inverse. With the Discrete Fourier Transform being $\mathcal{F}$, binding and unbinding are

$$C = A \circledast B = \mathcal{F}^{-1}\{\mathcal{F}A \odot FB\} \tag{1}$$

$$A \approx C \circledast B^{-1} = (A \circledast B) \circledast B^{-1}. \tag{2}$$

respectively (Eliasmith 2013; Dumont et al. 2023).

Spatial semantic pointers (SSPs) are an extension which enable the representation of continuous values. Specifically, SSPs can be used to represent spatial information (Komer et al. 2019).

For $k \in \mathbb{N}$, B^k is defined as

$$B^k = B \circledast B \circledast \ldots \circledast B \tag{3}$$

where B occurs k times. Extending this idea to continuous values simply means considering $k \in \mathbb{R}$. For HRRs, the computation above is then equivalent to

$$B^k = \mathcal{F}^{-1}\{\mathcal{F}\{B\}^k\} \tag{4}$$

which is a valid operation. This operation then allows for the representation of continuous values (Komer et al. 2019).

A more specific formula for SSPs is given by

$$\phi(x) = \mathcal{F}^{-1}\{e^{iAx}\} \tag{5}$$

where A is a matrix which is used to take a variable x and encode it as a SSP $\phi(x)$ (Dumont et al. 2023)

Previous work has shown that a specific choice of matrix A results in SSPs which result in grid-cell like patterns of activities in neurons. This hexagonally gridded representation can further be used to get place cell-like activity (Dumont and Eliasmith 2020).

In the 2-dimensional case, which I limit this paper to, the hexagonal activity results from considering equilateral triangles. Thus, the rows of the matrix are 2-dimensional unit vectors v_1, v_2, v_3 which are the corners of an equilateral triangle and centred around the origin. As noted above, the inverse DFT can be used to obtain the SSP for a location x. Thus, to have real valued locations, the SSP should display conjugate symmetry. If v_1, v_2, v_3 are the first three rows of the matrix A, the last three rows should then be $-v_1, -v_2, -v_3$. Applying different scaling and rotation to these vectors results in different scales and rotations of grids. Also, although I limit this project to 2 dimensions, this idea extends to higher dimensions (Dumont and Eliasmith 2020).

2.2 Localization

The LM of the NeuralSemantic SLAM is composed of a PI model and grid cells, which both maintain SSPs. The SSP represented by the PI network is the estimate, and the grid cells encode a cleaned-up SSP of this estimate (Dumont et al. 2023).

The PI model is composed of neuron populations which each encode the real and imaginary parts of the Fourier coefficients of the SSP representation. Since the location being encoded is real, there is conjugate symmetry in the Fourier coefficients, and so only half the coefficients need to be encoded. The input to the PI model is velocity, which has been encoded as an SSP. Previous work has shown that the resulting dynamics equation is

$$\frac{d}{dt}\begin{bmatrix} \text{Re}\mathcal{F}\{\phi(x)\}_j \\ \text{Im}\mathcal{F}\{\phi(x)\}_j \end{bmatrix} = \begin{bmatrix} 0 & -\omega_j \\ \omega_j & 0 \end{bmatrix}\begin{bmatrix} \text{Re}\mathcal{F}\{\phi(x)\}_j \\ \text{Im}\mathcal{F}\{\phi(x)\}_j \end{bmatrix} \tag{6}$$

This differential equation corresponds to a simple harmonic oscillator where the j-th coefficients of the SSP oscillate at frequency ω_j. Note that the frequency ω_j is the multiplication

5

of the velocity vector by the phase matrix. Thus, these neuron populations are VCOs, storing both the frequency and the real and imaginary part of the Fourier coefficients (Dumont et al. 2022; Dumont et al. 2023).

Previous work has added attractor dynamics for stability to get that

$$\frac{d}{dt}\begin{bmatrix} \text{Re}\mathcal{F}\{\phi(x)\}_j \\ \text{Im}\mathcal{F}\{\phi(x)\}_j \end{bmatrix} = \begin{bmatrix} -\omega_j\text{Im}\mathcal{F}\{\phi(x)\}_j + \frac{1-r_j^2}{r_j^2}\text{Re}\mathcal{F}\{\phi(x)\}_j \\ -\omega_j\text{Re}\mathcal{F}\{\phi(x)\}_j + \frac{1-r_j^2}{r_j^2}\text{Im}\mathcal{F}\{\phi(x)\}_j \end{bmatrix} \tag{7}$$

where $r_j = |\mathcal{F}\{\phi(x)\}_j|$. These equations have been derived in previous work (Dumont et al. 2022; Dumont et al. 2023).

The output of the PI model is cleaned up by taking the similarity between the output position SSP and a number of SSPs which have been sampled from a grid. This method is one possible cleanup method. Other methods include using a neural network or spiking neural network (Voelker et al. 2021). To focus on testing coupling methods, the similarity computation was picked for simplicity.

This "cleaned-up" output of the PI model is the input to the grid cells. The grid cells take in triplets of three Fourier coefficients which have been shown in previous PI models using these SSPs to demonstrate grid cell-like firing pattern.

I use the PI model from the NeuralSemantic SLAM system (https://github.com/nsdumont/ Semantic-Spiking-Neural-SLAM-2023) (Dumont et al. 2023) as a start for my experiments. The general format of the PI network and grid cells is laid out in Figure 1.

2.3 Coupling Mechanisms

The change that I make is to introduce coupling mechanisms between the VCOs and the grid cells to attempt to increase the stability of the model. As noted in the introduction, coupling between VCOs and grid cells has been suggested to match biological data. Membrane potential oscillators (MPOs) have been measured from the EC, and are not very stable. However, these MPOs may be stable due to connection to other VCOs (Burgess and Burgess 2014). There have also been theories on how oscillators exist in the brain, such as in networks with recurrent connections (Orchard et al. 2013).

Regardless, both of these hypotheses require mechanisms that minimize the drift of VCOs.

2.3.1 Coupling VCO Triples

For each triple of Fourier coefficients corresponding to a grid above, denoted $a_{i_1}, a_{i_2}, a_{i_3}$, their sum must be 0, since these coefficients correspond to directions at $120°$ of each other. That is, $a_{i_1} + a_{i_2} + a_{i_3} = 0$. The corresponding Fourier coefficients are $\Phi(x)_{i_1} = e^{ia_{i_1}\cdot x}$, $\Phi(x)_{i_2} = e^{ia_{i_2}\cdot x}$ and $\Phi(x)_{i_3} = e^{ia_{i_3}\cdot x}$ (N. S.-Y. Dumont, personal communication, March 1, 2024).

I test two coupling mechanisms which are suggestions by N. S.-Y. Dumont (personal communication, March 1, 2024).
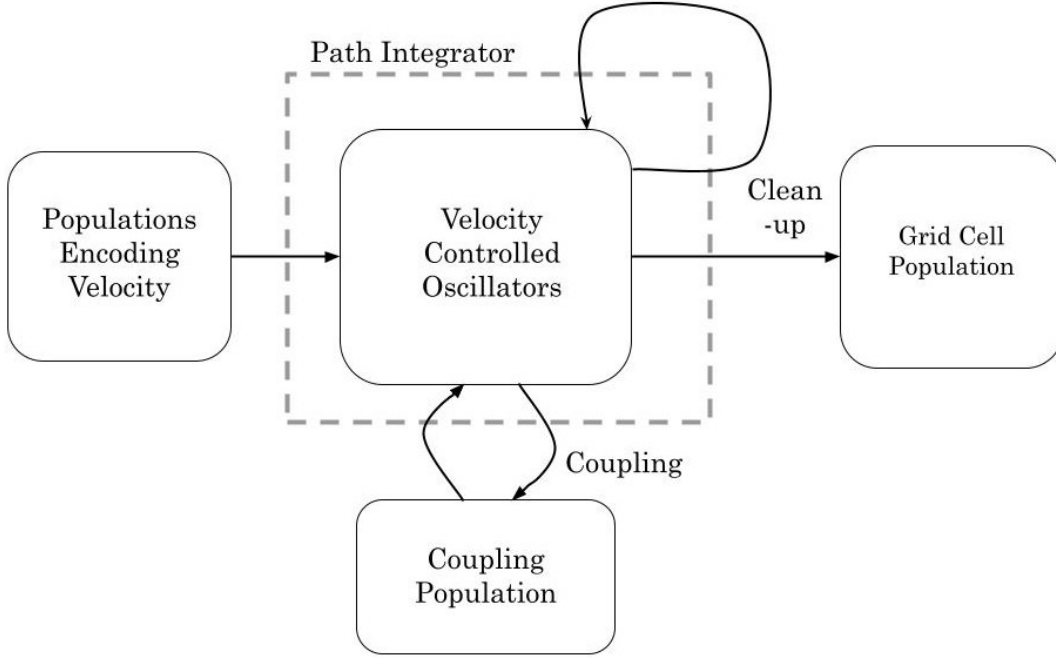
Figure 1: The general format of the PI network, grid cell population and coupling populations.

The first coupling mechanism is based on the fact that

$$(a_{i_1} + a_{i_2} + a_{i_3}) \cdot x = a_{i_1} \cdot x + a_{i_2} \cdot x + a_{i_3} \cdot x = 0. \tag{8}$$

But, $a_{i_\ell} \cdot x$ is the phase of the Fourier coefficient. Then, by the equation above, $a_{i_3} \cdot x$ (where which coefficient to consider is arbitrary) can be estimated as:

$$a_{i_3} \cdot x \approx -a_{i_1} \cdot x - a_{i_2} \cdot x = -\text{atan2}(\text{Im}\Phi_{i_1}, \text{Re}\Phi_{i_1}) - \text{atan2}(\text{Im}\Phi_{i_2}, \text{Re}\Phi_{i_2}). \tag{9}$$

Applying trigonometric identities, the estimate for $a_{i_3} \cdot x$, $\widehat{a_{i_3} \cdot x}$, is

$$\widehat{a_{i_3} \cdot x} \approx -\text{atan2}(\text{Im}\Phi_{i_1}\text{Re}\Phi_{i_2} + \text{Im}\Phi_{i_2}\text{Re}\Phi_{i_1}, \text{Re}\Phi_{i_1}\text{Re}\Phi_{i_2} - \text{Im}\Phi_{i_1}\text{Im}\Phi_{i_2}). \tag{10}$$

I use this estimate as a correction factor. Specifically, consider

$$\Delta a_{i_3} \cdot x = \widehat{a_{i_3} \cdot x} - a_{i_3} \cdot x. \tag{11}$$

I update $a_{i_3} \cdot x$ with $a_{i_3} \cdot x + \lambda \Delta a_{i_3} \cdot x$ where λ is a value in $[0, 1]$ that denotes how much to error correct. I pick 0.1 for this factor, although other values also work.

To do this update, note that $\Phi(x)_{i_3} = e^{ia_{i_3} \cdot x}$ is stored in the third neuron population. Thus, multiplying (in polar coordinates) the current stored value with $e^{i\lambda \Delta a_{i_3} \cdot x}$ yields

$$\Phi(x)_{i_3} \leftarrow e^{i\left(a_{i_3} + \lambda \Delta a_{i_3}\right) \cdot x}. \tag{12}$$

7

This method always involves updating the same coefficient of the three Fourier coefficients in the triplet. Other possible corrections could involve different decision factors for deciding which triplet to update.

I refer to this first method as *tangent* coupling in the rest of the document.

For the second coupling mechanism, by the property above, the following holds:

$$\Phi_{i_1}\Phi_{i_2}\Phi_{i_3} = e^{i(a_{i_1}+a_{i_2}+a_{i_3})\cdot x} = 1. \tag{13}$$

Then, if the product of the Fourier coefficients is not 1, these coefficients can be shifted equally towards 1. Let $\varepsilon = \Phi_{i_1}\Phi_{i_2}\Phi_{i_3}$. Then,

$$\frac{\Phi_{i_1}}{\varepsilon^{1/3}}\frac{\Phi_{i_2}}{\varepsilon^{1/3}}\frac{\Phi_{i_3}}{\varepsilon^{1/3}} = 1. \tag{14}$$

Consider Φ_{i_ℓ} divided by $\varepsilon^{1/3}$ in polar coordinates. If $\varepsilon = \alpha + i\beta$, then:

$$\frac{\Phi_{i_\ell}}{\varepsilon^{1/3}} = \frac{(\alpha\mathrm{Re}\Phi_{i_\ell} - \beta\mathrm{Im}\Phi_{i_\ell}) + i\left(\alpha\mathrm{Im}\Phi_{i_\ell} - \beta\mathrm{Re}\Phi_{i_\ell}\right)}{\alpha^2 + \beta^2} \qquad \forall\, \ell \in \{1,2,3\}. \tag{15}$$

Then, this value can be used to perform the update

$$\Phi_{i_\ell} \leftarrow \Phi_{i_\ell} + \lambda\left(\frac{\Phi_{i_\ell}}{\varepsilon^{1/3}} - \Phi_{i_\ell}\right) \qquad \forall\, \ell \in \{1,2,3\}. \tag{16}$$

where once again, λ is a correction factor in $[0,1]$.

I refer to this second method as *triple* coupling in the rest of the document.

2.3.2 Coupling with the Fourier Shift Theorem

The final coupling mechanism is based on the suggestion that the brain uses Fourier coefficients, which enables the application of the Fourier Shift Theorem (Orchard et al. 2013).

Let a_k be the preferred direction of a VCO, which stores Fourier coefficients Φ_k. Consider the new Fourier coefficients Φ'_k after shifting by x. The Fourier Shift Theorem states that

$$\Phi'_k = \exp\left(-2\pi i\frac{a_k \cdot x}{N}\right)\Phi_k. \tag{17}$$

The shift is called a *phase ramp* since $-2\pi i\frac{a_k \cdot x}{N}$ is a linear function. For VCOs that have preferred directions which are evenly spaced, as in the VCOs encoding the triples of the SSP defined above, the change in phase should be linear (Orchard et al. 2013).

This idea leads me to the third coupling mechanism. As above, let $a_{i_1}, a_{i_2}, a_{i_3}$ denote the triple of Fourier coefficients corresponding to a grid in the SSP encoding.

For each such triple, I compute the average phase difference between the three Fourier coefficients, and use this average phase difference to rotate the Fourier coefficients toward the corrected estimates suggested by the average phase difference.

That is, I compute the phase differences between Φ_{i_1}, Φ_{i_2}, between Φ_{i_2}, Φ_{i_3} and between Φ_{i_3}, Φ_{i_1}. For $i_\ell, i_{\ell+1 \mod 3}$, the phase difference is

$$c_\ell + is_\ell = \exp(i(a_{\ell+1} - a_\ell) \cdot x) = \exp(ia_{\ell+1} \cdot x) \exp(ia_\ell \cdot x) \tag{18}$$

$$c_\ell + is_\ell = \Phi_{i_{\ell+1}} \cdot \overline{\Phi_\ell}. \tag{19}$$

Using equation (19), which was derived in Orchard (2013) I compute the phase differences and consider the average of this difference, $c + is$.

Given i_ℓ, $i_{\ell-1 \mod 3}$ and $i_{\ell+1 \mod 3}$, I then can obtain estimates by rotating the previous vector clockwise and the next vector counterclockwise. That is, I get estimates

$$\widetilde{\Phi}_{i_\ell}^{(1)} = \Phi_{i_{\ell-1 \mod 3}}(c - is) \tag{20}$$

$$\widetilde{\Phi}_{i_\ell}^{(2)} = \Phi_{i_{\ell+1 \mod 3}}(c + is). \tag{21}$$

I can then compute the difference between these estimates and the actual Fourier coefficient being encoded as

$$\Delta\Phi_{i_\ell} = \frac{1}{2}\widetilde{\Phi}_{i_\ell}^{(1)} + \frac{1}{2}\widetilde{\Phi}_{i_\ell}^{(2)} - \Phi_{i_\ell}. \tag{22}$$

Then, for a correction factor $\lambda \in [0, 1]$, I update

$$\Phi_{i_\ell} \leftarrow \Phi_{i_\ell} + \Delta\Phi_{i_\ell}. \tag{23}$$

I refer to this method as *phase shift* coupling in the rest of the document.

While the update method is different, the underlying idea of this coupling mechanism is similar to the tangent coupling mechanism presented in Section 2.3.1. This mechanism uses that the preferred direction of the VCOs differs by 120°. However, this mechanism can be extended to more VCOs.

The original experiments with this coupling mechanism had 17 VCOs with equally spaced phases connected in pairs to obtain an average of the phase difference (Orchard et al. 2013). Having more VCOs with equally spaced VCOs would most likely result in a better average of phase difference, and thus a better update. Future work may explore this coupling mechanism further. However, changes to obtain equally spaced VCOs would involve modifying the phase matrix of the SSP above, which would probably also require more dimensions to obtain an accurate encoding of position. This exploration is left as future work.

2.4   Experiments and Analysis

The goal of this experiment is to test the three coupling mechanisms laid out above, compared to the LM without any coupling mechanisms. For all experiments, I include both the PI model, with or without coupling mechanisms, as well as the grid cell output population. As noted in Section 2.1, I sample points on a grid and compute the similarity between the output and these sample points as the clean-up method.

The LM is built with Nengo (www.nengo.ca). I initially started with the PI model from the NeuralSemantic SLAM and made the modifications noted above (Dumont et al. 2023).

I use the parameters in Table 1 unless otherwise specified.

Parameter	Default Value
VCO Population Neurons	700
Grid Cell Population Neurons	1000
Domain Dimension	2
SSP Dimension	151
Post-synaptic Time Constant	0.05
Error Correction Factor	0.01

Table 1: Default parameters used for experiments with the LM and coupling mechanisms.

As in previous works on the PI model, I generate random paths to ensure enough neuron activity. These random paths are generated from "band-limited white noise signals" (Dumont et al. 2023). The velocity is computed from these paths.

I want to see whether the coupling mechanisms improve the accuracy of the LM. Thus, for the base model and for each coupling mechanism, I test the model on 10 randomly generated paths for 30 s.

To determine the accuracy of the LM, I compute the distance from the model's estimate to the true value of the path at each timestep. (Note that this value is the RMSE for one data point, as at each point I consider the absolute value of the distance from the origin.) This error as the absolute error, as in Dumont et al. (2023).

To get the error over the simulation, I integrate the distance between the model's estimate and the true path over the length of the simulation. Here, I refer to this error as the integrated error. To measure the variance in these values, I compute the standard deviation over the results from my trials.

This experiment allows me to compare the amount of error that accumulates from running the base PI model compared to the amount of error that accumulates while running the coupling mechanisms. This experiment thus reveals whether the coupling mechanisms improved the stability of the LM or not.

To further test the changes with the coupling mechanisms, I run the models on 5 randomly generated paths for 30 s while varying the number of neurons in the PI model. With more neurons in the VCOs of the PI model, the original PI model becomes more stable (Dumont et al. 2023). For a coupling mechanism to be successful, I would like to observe a similar result for any of the coupling mechanisms. That is, with more neurons, the coupling mechanism should further reduce the drift in the estimated path. Moreover, I can check if adding a coupling mechanism to the PI model results in the same accuracy but with fewer neurons in the population. This result would suggest that the coupling mechanism improved the accuracy of the LM.
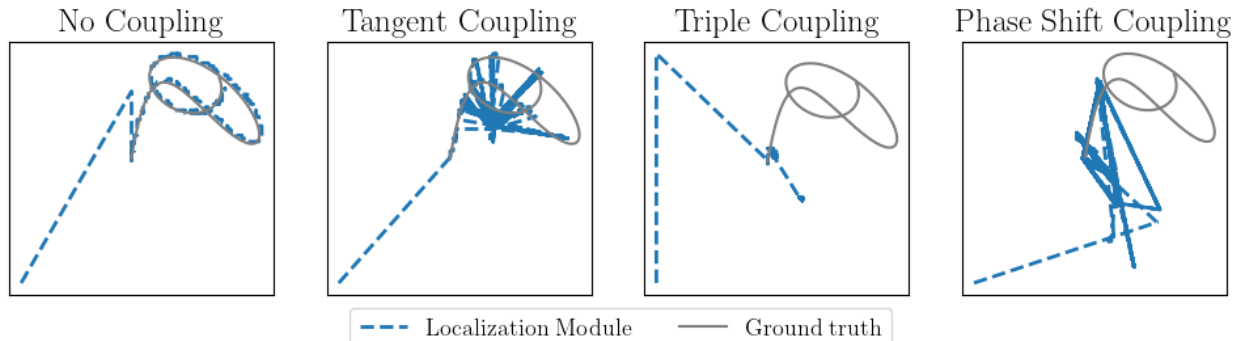
Figure 2: Example of the LM without coupling and with the three different coupling mechanisms on a 30 s long path.

Finally, I check the activity of the grid cells as a qualitative test of performance. In previous work, the grid cells of the LM have produced grid-cell like activity (Dumont and Eliasmith 2020; Dumont et al. 2023). I check if this grid cell-like activity results from the grid cells of the base LM and of the LMs with added coupling mechanisms.

To perform the qualitative test, I perform path integration outside of Nengo and encode each predicted value as a SSP in a population of grid cells. The neurons in the grid cell population should display grid cell-like activity over the course of the simulation. I compare the resulting activity to the activity of the grid cells in the models in the middle and at the end of my simulation, to see how similar or different the activities are.

The goal of this qualitative test is to ensure that the grid cells are still producing grid cell-like activity, which is necessary to ensure that the model is satisfying the constraints placed on spatial navigation systems by biology.

3   Results

Figure 2 displays sample outputs of the LM without coupling and with the three coupling mechanisms - tangent coupling, triple coupling and phase shift coupling. These samples are from running the LM on a path which is 30 s long. Even from these samples, I can see that the coupling mechanisms do not perform as well as the LM without coupling.

As noted in Section 2.4, the statistical measures I use are the absolute error and the integrated error. The absolute error is the average distance of the estimate of the model from the true path over all the timesteps, while the integrated error is obtained by integrating the distance from the true path over time. As a consequence, the integrated error and absolute error are very similar. The absolute error without coupling is 0.0292 ± 0.0053, compared to 0.2643 ± 0.0495 with tangent coupling, 0.9570 ± 0.1705 with triple coupling and 0.9592 ± 0.1316 with phase shift coupling. These values are proportional to the integrated errors plotted in Figure 3.

Figure 3 displays the integrated error for the LM without coupling mechanisms and with the three coupling mechanisms. The LM without coupling mechanisms has lower integrated error
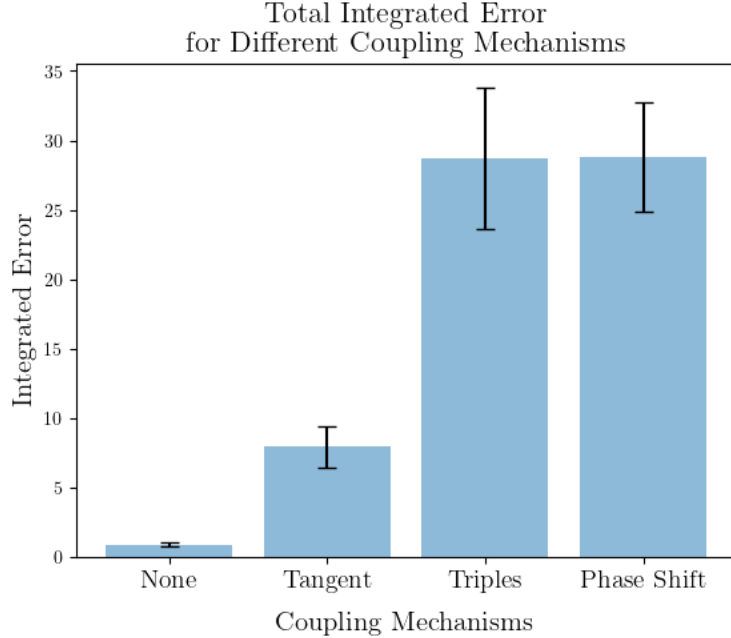
Figure 3: The average integrated error over each 30 s trial for the different coupling mechanisms. The standard deviation is computed from the error of the 10 trials.

(and absolute error) compared to any of the LMs with coupling mechanisms. The tangent coupling mechanism has the second lowest integrated error (and absolute error), while the phase shift coupling mechanism and triple coupling mechanism have similar integrated error (and absolute error).

These results suggest that the LM without coupling performs better than the LMs with coupling. While this result counters the original predictions, this results aligns with the results of the sample paths I see above.

One of my initial predictions was that coupling mechanisms may help improve the LM when there are fewer neurons in the VCO population.

Figure 4 displays the absolute and integrated error plotted against the number of neurons. The absolute and integrated error for the LM decreases and is the lowest, as expected given the data above. Similarly, the tangent coupling mechanism is second lowest, while the phase shift and triple coupling mechanisms have the greater absolute and integrated error again.

However, one interesting result is that as the number of neurons in the VCO populations increase, the absolute and integrated error do not decrease for the phase shift and triple coupling mechanisms. This result suggests that these coupling mechanisms do not help with the drift of the LM.

One limitation of these results is that 30 s paths were used. When running the LM for longer, the LM on its own eventually drifts significantly from the true path (Dumont et al. 2023). From the sample paths in Figure 2, I see that the 30 second path might not be long enough
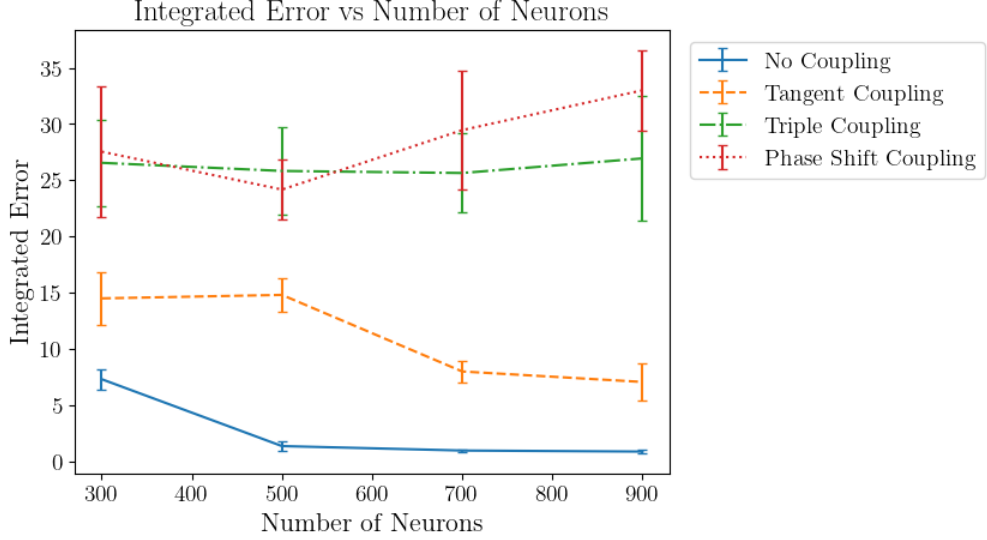
Figure 4: The average integrated error over each 30 s trial for the different coupling mechanisms, plotted against the number of neurons. The tests were run with 300, 500, 700 and 900 neurons in the VCO population. The standard deviation is computed from the error of 5 trials.

to see this result in my data. However, from Figures 3 and 4, the 30 s long paths are enough to compare the performance of the coupling mechanisms to the original LM. Indeed, from looking at sample paths in Figure 2 and the errors in Figures 3 and 4, these results suggest that the coupling mechanisms may be overcorrecting before error accumulates.

Finally, I plot the activity of a neuron in the grid cell population on a random path which is 120 s long. In previous work, this neuron has displayed grid cell-like activity. However, for the PI model without correction from a SLAM system, there is increased noise in the model over time (Dumont et al. 2023).

In Figure 5, I compare the activity of a neuron in the grid cell population of the LM with and without coupling mechanisms to grid cells which are encoding the SSP for a path estimate obtained from integrating over the velocity. I use a random path, which limits the extent to which the path covers the environment.

However, from this data, I can see some evidence of a grid cell-like activity pattern in the spikes of the grid cell from the reference PI. The spikes from the grid cell from the LM without coupling look similar to the spikes from the reference PI, although there may be some added noise over time.

The spikes of the LM with coupling do not resemble the grid cell-like activity of the reference PI. Grid cell activity may be occurring in the phase shift coupling mechanisms and perhaps the triple coupling. However, due to the difference between paths outputted from these coupling mechanisms and the provided path, it is challenging to be able to draw a conclusion about the grid cell activity.
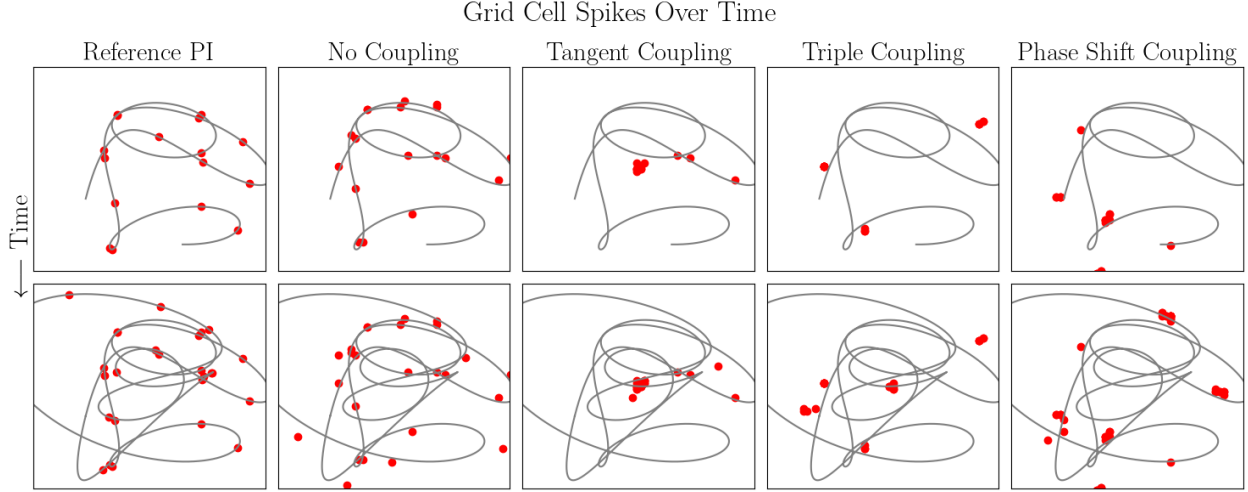
Figure 5: Spikes recorded from a neuron in the grid cell population of the LM with the corresponding coupling mechanism. The reference PI is a population of grid cells which encode the SSP of a path estimate from integrating the velocity over time. The spikes are plotted as red dots at the location estimate of the grid cell population at the time of the spike. The path is included as reference on the plot. The top row of figures is the path and grid cell recordings after running the LM on a random path for 60 s. The bottom row of figures is the path and grid cell recordings after running the LM on the entire random path for 120 s.

Interestingly, tangent coupling, which has the lowest error of the coupling mechanisms, appears to have the activity which is the least similar to grid cell activity.

The code for the models and experiments can be found at https://github.com/aliciabremer/syde-552-project.

4   Discussions

From the experiments above, the results suggest that the coupling mechanisms that I implemented did not help with reducing the drift of the LM. Indeed, the coupling mechanisms appear to make the LM perform much worse, as the LM fails to maintain a correct estimate of the path.

Of the coupling mechanisms, tangent coupling had the lowest error. The tangent coupling mechanism involved only updating one of the three Fourier coefficients which define a triangular grid. The other two coupling mechanisms, triple coupling and phase shift coupling, involve updating all three coefficients which correspond to a triangular grid.

Moreover, with the coupling mechanisms, the grid pattern of the neurons in the grid cell population is not maintained as clearly, which further suggests that these coupling mechanisms may not be effective.

There is clear neuroscience evidence of grid-like firing patterns from grid cells in the EC, and

14

so this firing pattern is ideally maintained with any successful coupling mechanism. For all the coupling mechanisms I tested, it is unclear whether the firing pattern is maintained, which may in part be due to significant error in the resulting paths of the coupling mechanisms. Regardless, further improvements to the coupling mechanisms to both reduce the error and better test the grid cell-like firing pattern is required to conclude that a coupling mechanism is effective.

Moreover, I noted in the introduction that the number of grid cells in the EC outnumbers the number of cells sensitive to velocity. In Figure 4, I compare the error without coupling and with each coupling mechanism for a varying number of neurons. With no coupling, the error is much lower, and decreases as the number of neurons increases, although the decrease from 500 to 900 neurons is minimal.

The error with tangent coupling also appears to decrease somewhat as the number of neurons increase. However, the error for phase shift coupling and triple coupling do not really decrease. These results suggest that these last two coupling mechanisms may be resulting in a wrong path estimate, as the error is expected to decrease as the number of neurons of the VCO population increases.

Overall, from these results, there do not appear to be any generated hypotheses about the distribution of neurons in the EC.

While the results are disappointing, I did not expect that the coupling mechanisms would be the most effective. In the tangent coupling method, I update only one of the three Fourier coefficients, and the one that is updated is fixed. I expected that this method would not perform well. While the error was indeed greater than without coupling, I was surprised that the error was less with this method than with triple coupling.

In triple coupling, I expected the error to be decreased since each of the Fourier coefficients is shifted by the constraints given by the grid cell-like representation. However, upon further thought, updating all three coefficients may result in additional dependencies between the coefficients, resulting in incorrect paths.

With phase shift coupling, I did not expect great results as the original implementation had 17 VCOs in sequence, instead of 3. However, I did expect some level of accuracy, which did not seem to be present.

To summarize, I found the following:

1. The error in the LM was greater with the coupling mechanisms than without any coupling mechanisms in my experiments, with tangent coupling performing the best of the three coupling mechanisms presented

2. As the number of neurons increases, the error for the LM without coupling and with the tangent coupling mechanism decreases.

3. Further improvement of the coupling mechanisms is required to perform a better qualitative analysis of the spiking activity of the neurons in the grid cell populations. Currently, it is difficult to determine whether a grid-like pattern is maintained, in part probably due to the error in the path integration.

Future work may look at improving these coupling mechanisms by reducing the amount of correction. The LM remains accurate at the start of the trial, although eventually drifts from the path estimate. With the coupling mechanisms, the path estimate in the sample paths appears to differ from the true path from the start. Possible work may look into ways to integrate the coupling mechanisms such that the path estimate is only updated occasionally, although how and when the updates occur would need to be determined.

When looking at phase shift coupling, I noted that the original implementation used 17 equally spaced VCOs (Orchard et al. 2013). In the phase matrix for the SSPs, different grids are obtained by random rotation and scaling (Dumont et al. 2022). To integrate these methods, one possible change would be to fix the rotations to obtain a greater number of VCOs with preferred directions equally spaced around a unit circle. A higher dimensional SSP may be required to maintain an accurate representation of location.

Overall, I expect that this change would reduce overcorrection within the triples of the Fourier coefficients. I would implement this coupling mechanism next, as it naturally builds on the work done here.

There may also be more coupling mechanisms which use feedback from the grid-cell population, which stores a cleaned-up SSP for the location.

In addition to more coupling mechanisms, future work may also explore other areas of the network that could be improved by using the relationship between the Fourier coefficients of the SSP representation. In the introduction, I noted that there are different cleanup methods for the SSPs, which include spiking neural networks (Voelker et al. 2021). There may be ways to devise better measurements of error based on the relations within the Fourier coefficients of the SSP, to improve the accuracy of these networks. Future work may involve brainstorming and experimenting whether such a change would be feasible and beneficial.

While the coupling mechanisms presented here were largely unsuccessful, there is still room for improvement. These future changes, as well as others, may reveal how coupling mechanisms can be used to improve the accuracy of the path estimate.

5 Acknowledgements

References

Boccara, C. N., Sargolini, F., Thoresen, V. H., Solstad, T., Witter, M. P., Moser, E. I., & Moser, M.-B. (2010). Grid cells in pre- and parasubiculum. *Nature neuroscience*, *13*(8), 987–994. doi:10.1038/nn.2602

Burgess, C. P., & Burgess, N. (2014). Controlling phase noise in oscillatory interference models of grid cell firing. *Journal of Neuroscience*, *34*(18), 6224–6232. doi:10.1523/JNEUROSCI.2540-12.2014

Burgess, N. (2008). Grid cells and theta as oscillatory interference: Theory and predictions. *Hippocampus*, *18*(12), 1157–1174. doi:https://doi.org/10.1002/hipo.20518

Dumont, N. S.-Y., & Eliasmith, C. (2020). Accurate representation for spatial cognition using grid cells. In *42nd annual meeting of the cognitive science society* (pp. 2367–2373). Toronto, ON: Cognitive Science Society.

Dumont, N. S.-Y., Furlong, P. M., Orchard, J., & Eliasmith, C. (2023). Exploiting semantic information in a spiking neural slam system. *Frontiers in Neuroscience*, *17*. doi:10.3389/fnins.2023.1190515

Dumont, N. S.-Y., Orchard, J., & Eliasmith, C. (2022). A model of path integration that connects neural and symbolic representation. In *Proceedings of the annual meeting of the cognitive science society* (Vol. 44), Toronto, ON: Cognitive Science Society.

Eliasmith, C. (2013). *How to build a brain: A neural architecture for biological cognition*. New York, NY: Oxford University Press.

Komer, B., Stewart, T. C., Voelker, A. R., & Eliasmith, C. (2019). A neural representation of continuous space using fractional binding. In *41st annual meeting of the cognitive science society*, Montreal, QC: Cognitive Science Society.

McNaughton, B. L., Battaglia, F. P., Jensen, O., Moser, E. I., & Moser, M.-B. (2006). Path integration and the neural basis of the 'cognitive map'. *Nature reviews. Neuroscience*, *7*(8), 663–678. doi:10.1038/nrn1932

Moser, E. I., Kropff, E., & Moser, M.-B. (2008). Place cells, grid cells, and the brain's spatial representation system. *Annual review of neuroscience*, *31*(1), 69–89. doi:10.1146/annurev.neuro.31.061307.090723

Orchard, J., Yang, H., & Ji, X. (2013). Does the entorhinal cortex use the fourier transform? *Frontiers in Computational Neuroscience*, *7*. doi:10.3389/fncom.2013.00179

Sargolini, F., Fyhn, M., Hafting, T., McNaughton, B. L., Witter, M. P., Moser, M.-B., & Moser, E. I. (2006). Conjunctive representation of position, direction, and velocity in entorhinal cortex. *Science*, *312*(5774), 758–762. doi:10.1126/science.1125572

Schmidt-Hieber, C., & Haeusser, M. (2013). Cellular mechanisms of spatial navigation in the medial entorhinal cortex. *Nature neuroscience*, *16*(3), 325–331. doi:10.1038/nn.3340

Voelker, A. R., Blouw, P., Choo, X., Dumont, N. S.-Y., Stewart, T. C., & Eliasmith, C. (2021). Simulating and predicting dynamical systems with spatial semantic pointers. *Neural Computation*, *33*(8), 2033–2067. doi:10.1162/neco_a_01410